Supporting Information

Darrah et al. 10.1073/pnas.1322107111

SI Text

Geological Background. ***Northeastern Pennsylvania (Marcellus).*** The Appalachian Basin is an archetypal energy-producing foreland basin (Fig. S1) located in the northeastern United States. In the eastern part (northeastern Pennsylvania and southern New York) of the northern Appalachian Basin (NAB), oil and gas production occurs within various lithologies throughout the northern Appalachian Plateau region, but is largely confined to two genetic groups: (*i*) migrated gases sourced from Ordovician (~485–443 Ma) shales and hosted in Ordovician/Silurian (~443–419 Ma) tight sands and carbonates of the Trenton/Black River and (*ii*) Middle Devonian (~384–377 Ma) source/reservoir tight gas black shales of the Marcellus Group (1). More complete descriptions of relevant Appalachian geology and hydrocarbon potential in this area are available elsewhere (1–4).

The structural architecture of the NAB evolved throughout the Taconic, Acadian, and Alleghanian orogenies, all of which deposited and deformed the sedimentary rocks throughout the basin (5–8). Today, the complex depositional and tectonic history of this area is visible within the northern section of the Appalachian Plateau physiographic province whose gently dipping strata contain salt-cored detachment folds and are further deformed by layer parallel shortening, reverse faults, and fracturing (7–9).

Select lithologies of interest in the study area include the following: the Middle Ordovician Trenton/Black River Group, the Upper Silurian Salina Group, the Middle Devonian-aged Hamilton Group (~393–388 Ma), and the Upper Devonian Brallier (~385–375 Ma), Lock Haven (~375–369 Ma), and Catskill Formations (~369–359 Ma) (Fig. S2). The interbedded limestones and shales of the Trenton/Black River Group and the overlying organic-rich Utica shale represent Taconic orogenic sediments (10). The Salina Group consists of interbedded shales, dolomites, and salt deposits that act as the regional decollement for Alleghanian structures (8, 11). As a result, structural folds and faults above the decollement (i.e., Devonian and younger stratigraphic units) bear little resemblance in deformation style or hydraulic connectivity to those present beneath the Salina Group (8, 11).

The Hamilton Group is a wedge of marine sediments that is thicker to the east and south and includes the organic- and siliciclastic-rich, hydrocarbon-producing Marcellus subgroup at its base (12, 13). Rb-Sr age dating suggests that the deposition of the Marcellus Formation occurred from ~384 ± 9 to 377 ± 11 Ma (14, 15). The Upper Devonian consists of thick synorogenic deposits including the Brallier, Lock Haven, and Catskill Formations (Fig. S2). The latter two formations constitute the two primary lithologies that serve as groundwater aquifers in the Marcellus Study Area (MSA) in northeastern Pennsylvania and southern New York, along with the overlying glacial and sedimentary alluvium (16).

The Hamilton Group and other formations above the Salina slid along the weak Salina salt as part of the Appalachian Plateau detachment sheet (8, 9). Deformation within the Appalachian plateau detachment sheet is significantly less intense than the Valley and Ridge province and shows a combination of layer parallel shortening, folding that leads to the broad anticline/syncline sequences, duplex/thrust faulting structures, and jointing (e.g., J_1 and J_2) (4, 8, 14). Each of these deformation features exists within our study area. A combination of thrust load-induced subsidence, clastic loading, and Alleghanian deformation induced thermal maturation and eventually catagenesis and metagenesis within the Marcellus Formation (4, 17). In the NAB, Alleghanian deformation also led to large-scale migration of hot, deep formational brines away from the hinterland and into the foreland (i.e., Appalachian Plateau) (18, 19).

Rifting of the Atlantic Ocean that began in the Mesozoic (e.g., Triassic basalts of Connecticut and New Jersey), accompanied by recent cycles of glacial advance and retreat, led to rapid exhumation/unloading, erosion, and neotectonic jointing (i.e., often termed J_3) in at least the top 0.5 km of the crust (20). The major Triassic rift basins in the Appalachian Basin occur in the Gettysburg–Newark lowland and offshore. Because these rift basins are on the opposite side of the Appalachian Structural Front, it is highly unlikely that these Triassic rifts made significant mantle contributions to the gas chemistry of the plateau region, specifically in our study area (i.e., >150 km away from rift basins). Note that all of our samples have purely crustal helium isotope ratios ($^3He/^4He$) and atmospheric neon isotope ratios ($^{20}Ne/^{22}Ne$ and $^{21}Ne/^{22}Ne$) that confirm a dearth of mantle contributions, which otherwise would be easily identifiable using our methods.

Pleistocene glacial cycles may also influence the permeability of aquifers within our study area. Ice loading and retreat led to an additional cycle of shallow crustal compaction, glacial isostatic rebound, and likely neotectonic fracturing within the MSA. As a result of both tectonic and glacial processes, previously deeply buried lithologies such as the Catskill and Lock Haven Formations are much closer to the surface today and often serve as highly naturally fractured, dual permeability aquifers for drinking-water supplies. The major stratigraphic sequences above the Upper Devonian Catskill Formation in our study area have eroded away and therefore are not discussed. More complete reviews of Carboniferous Age (Mississippian and Pennsylvanian) deposition in the NAB are available elsewhere (6).

East-Central Texas (Barnett). The Fort Worth Basin is an elongated north-south trending trough that covers ~38,000 km^2 throughout northeastern-central Texas in the southern United States (Fig. S1). The basin consists of Paleozoic sedimentary rocks within an asymmetric, wedge-shaped sedimentary package that is ~3,700 m deep along the western portion of the Muenster Arch (21–23). The Fort Worth Basin was a foreland basin that formed in response to the thrusting of the Ouachita structural belt (21) onto the North American continental margin during the Ouachita-Marathon orogeny in the late Mississippian (~359–323 Ma) through the early Pennsylvanian (~323–299 Ma) (21–24).

The structural geology of the Fort Worth Basin, which formed in response to the Ouachita orogeny, is complex and includes major and minor normal and thrust faults, folding, intense natural fractures, and karst-related terrains (21). The basin is bounded by the Ouachita structural front to the east and southeast, the Llano uplift to the south, the Muenster and Red River arches to the north and northeast, and the Bend Arch to the west (which represents a flexural and structural high) (24). One prominent fault within the basin is the poorly understood Mineral Wells basement fault that runs through Parker County, TX (northwest of our study area) (21, 24).

The Paleozoic sedimentary package contained within the Fort Worth Basin is underlain by a Precambrian granite and diorite basement (Fig. S3). The Paleozoic stratigraphic column (dominated by carbonates) was deposited along the stable continental cratonic shelf from the Cambrian to the Mississippian with interruptions caused by marked drops in sea level during the Silurian and Devonian. One example is the Ellenberger unconformity, which started during the Ordovician and prevented the deposition of Silurian rocks (25). Similarly, Permian sequences are less abundant, whereas no Triassic or Jurassic rocks have been found in the basin,

presumably as a result of erosion preceding the Cretaceous (21, 24, 25). The basin includes ~1,200–1,500 m of Ordovician-Mississippian carbonates and occasional interbedded shales, 1,800–2,100 m of Pennsylvanian clastics and carbonates, and a thin covering of Comanche series Cretaceous rocks (21).

Commercial oil and gas activities in the Fort Worth Basin over the last decade have focused on the Barnett Shale (26–28). The organic-rich Barnett Shale was deposited over the Ellenburger unconformity during the late Mississippian (~354–323 Ma) (21, 24, 25). The Barnett, which has a thickness of ~15 m along the western margin that increases to more than 305 m near the Muenster Arch, is the primary petroleum source rock in the Fort Worth Basin (21, 24, 26, 27, 29). In general, the Barnett Formation is oil prone in the northern and western portions of the basin, whereas thermal maturities are sufficient for wet gas generation to the south and east (24, 26, 29, 30). The geographic area included within the current study area in Parker County, TX [Barnett Study Area (BSA); Fig. S3] resides entirely within the gas window (i.e., wet gas window) (30). Because there is a minimal correlation between hydrocarbon maturity and in situ reservoir vitrinite reflectance values, many workers suggest that there was significant geological migration of hydrocarbons from the source rocks (i.e., the Barnett Formation in the Upper Mississippian) into the overlying Middle-Pennsylvanian Bend and Strawn Formations (~323–299 Ma) within the BSA (21, 24, 27, 31).

The principal aquifers of our study area in east-central Texas consist of a series of shallow marine Cretaceous formations, including the Trinity Group (or Trinity aquifer) (25, 32). The Trinity Group, which consists of limestone, calcareous sandstones, silts, and conglomerates, includes the Lower Trinity (e.g., Sycamore sandstone, Sligo Formation), the Hammett Shale, the Middle Trinity (Cow Creek limestone, Hensell sandstone), and the Upper Trinity (Glen Rose limestone) (25, 32). Based on sampling depths, our groundwater samples from east-central Texas are all collected from either the Middle or Upper Trinity aquifer (31, 32) (Fig. S3).

Materials and Methods. ***Sample selections in the Marcellus and Barnett regions.*** We examine the noble gas isotopic compositions of 113 domestic groundwater wells and one natural methane seep within an eight-county area of Pennsylvania (Bradford, Lycoming, Sullivan, Susquehanna, and Wayne counties) and New York (Broome, Delaware, and Sullivan counties) (Table S1). The MSA is within the NAB Plateau region underlain by the Marcellus Shale (~800–2,200 m depth; Figs. S1 and S2). Drinking-water wells in our study had typical depths of 35–90 m and were sourced in either fractured sandstone of the Lock Haven or Catskill Formation or the outwash alluvium contained in river valleys. We integrate noble gas, hydrocarbon (i.e., the molecular and isotopic composition of hydrocarbon gas), and dissolved inorganic constituent (i.e., Cl^-) data with previous work on the principal aquifers of the region (Alluvium, Catskill, and Lock Haven) (33, 34).

We hypothesized that diagnostic isotopic ratios (e.g., $^4He/CH_4$, $^{20}Ne/^{36}Ar$, and $\delta^{13}CH_4$) and molecular abundances (e.g., $[CH_4]$, $[^{20}Ne]$, $[^{36}Ar]$, and $[N_2]$) would allow us to differentiate between samples with elevated methane concentrations resulting from the natural geological migration of hydrocarbon gas and those that result from fugitive gas contamination in the MSA. Therefore, we adjusted our previous sampling methodologies, which did not target houses with high methane concentrations in their water, to include by design a subset of water wells known to have elevated methane both near (<1 km) and away (>1 km) from drilling. These water wells allowed us to examine the cause for the high methane concentrations observed, distinguishing among natural and anthropogenic mechanisms.

We present data from this study according to their distance from shale-gas well sites at the time of sampling. Samples from MSA collected >1 km from drilling are displayed as triangles, whereas samples <1 km from drilling sites are displayed as circles. The saline spring at Salt Spring State Park, Montrose, PA, is shown as a square, and samples targeted for their microbial inputs are shown as diamonds in Figs. 2–4 and Figs. S7 and S8. Within all figures, the abundance of methane is preserved using grayscale intensity where methane concentrations of 0 cm^3 standard temperature and pressure (STP)/L are white and range up to black for >60 cm^3 STP/L. In the MSA, we compare groundwater data to published data from production wells across the plateau region of the NAB (35–39).

Data from producing conventional (i.e., vertical) well in the MSA were collected and reported in ref. 37. These data are presented in Table S3.

To test the geochemical framework we developed for the Marcellus in a different shale formation, we studied groundwater and produced gas samples in the Barnett Formation of Texas as well (Table S2). Elevated levels of methane in a subset of domestic groundwater wells at this site have been the source of substantial controversy (31). We analyzed groundwater samples from 20 domestic drinking-water wells near the city of Weatherford in Parker County, TX (Figs. S1 and S3).

The BSA is within the Fort Worth Basin underlain by the Barnett Shale (~1,800–2,500 m depth; Fig. S3). The typical depth of drinking-water wells in the study area was 60–75 m. In Parker County, TX, groundwater samples collected <1 km from active drill sites are plotted as circles, whereas those samples collected >1 km from active drill sites are plotted as inverted triangles in Figs. 2–4 and Figs. S4–S6. In all plots from BSA, the abundance of methane is preserved using a grayscale intensity where white corresponds to methane concentrations of 0 cm^3 STP/L and ranges up to black for >60 cm^3 STP/L.

Data from Parker County hydrocarbon gas production wells were collected from producing conventional (i.e., vertical) wells as part of the current study according to methods described previously (37). Sample intervals include the Barnett and Strawn Formations. These data are presented in Table S3.

Sample analyses. All groundwater samples in the MSA and BSA (n = 134) were analyzed for their major gas abundance (e.g., CH_4, C_2H_6, C_3H_8, N_2, and O_2) and noble gas elemental ([He], [Ne], and [Ar]) and isotopic ($^3He/^4He$, $^{20}Ne/^{22}Ne$, $^{21}Ne/^{22}Ne$, $^{38}Ar/^{36}Ar$, $^{40}Ar/^{36}Ar$, and $^{20}Ne/^{36}Ar$) composition according to standard methods reported previously (37, 40). All groundwater samples for noble gas analyses were collected and simultaneously measured for hydrocarbon molecular and stable isotopic composition and dissolved inorganic constituents (i.e., Cl^-) (33, 34). The stable carbon isotopic compositions of methane ($\delta^{13}C\text{-}CH_4$) were determined for all samples with $[CH_4]$ exceeding 0.5cm^3 STP/L, whereas the stable carbon isotopic composition of ethane ($\delta^{13}C\text{-}C_2H_6$) is available for a subset of samples with $[C_2H_6]$ exceeding ~0.1 cm^3 STP/L.

Before sampling, wells were flowed to remove stagnant water and simultaneously monitored for pH, electrical conductance, and temperature until stable values were obtained. Water samples were collected before any treatment systems and were filtered and preserved using US Geological Survey (USGS) protocols (41). The methods for the analyses of inorganic constituents (e.g., Cl^-) were identical to those reported previously (33, 34). Dissolved gas samples were collected in the field using procedures detailed by Isotech Laboratories (42), stored on ice until delivery to their facilities, and analyzed for the concentrations of methane, ethane, and propane and the carbon isotopic compositions of methane and ethane. Procedures for stable isotope analyses of gas are summarized in Osborn et al. (34). Isotech Laboratories uses chromatographic separation followed by combustion and dual-inlet isotope ratio MS to measure dissolved gas concentrations and stable isotopic composition [detection limits for methane (CH_4), ethane (C_2H_6), and propane (C_3H_8) were 0.001, 0.0005, and 0.0001 mol %, respectively].

Noble gas samples were collected in refrigeration-grade copper tubes that were flushed in-line with at least 50 volumes of sample water before sealing with stainless steel clamps (43). In the laboratory, the fluid (~25 cm^3) was extracted from the copper tube on a vacuum line and sonicated for ~30 min to ensure complete transfer of dissolved gases from the extraction vessel to the sample inlet line (43, 44). Major gas components (i.e., N_2, O_2, Ar, and CH_4) were measured using a Dycor quadrupole MS and a SRI GC (37, 40). The isotopic analyses of noble gases were performed using a VG 5400 MS at the University of Rochester Rare Gas Facility. Standard analytical errors were ±3% for noble gas concentrations ([^{4}He], [^{22}Ne], and [^{40}Ar]). Isotopic errors were approximately ±0.01 times the ratio of air (or 1.4×10^{-8}) for ^{3}He/^{4}He ratio, <±0.5% and <±1% for ^{20}Ne/^{22}Ne and ^{21}Ne/^{22}Ne, respectively, and <±1% for ^{38}Ar/^{36}Ar and ^{40}Ar/^{36}Ar (higher than typical because of interferences from C_3H_8 on mass = 36 and 38).

Genetic classification of hydrocarbon gases. Within the context of petroleum geochemistry, hydrocarbon gases are typically classified as thermogenic, biogenic, or mixed, with the distinction typically based on their molecular and isotopic composition (e.g., δ^{13}C-CH_4) (45). Biogenic gas is generated at low temperatures («100 °C) in anoxic or hypoxic conditions from the microbial decomposition of organic matter and/or the reduction of CO_2 (46). Microbes produce methane gas almost exclusively [i.e., methane/ethane plus higher order hydrocarbons (CH_4/C_2H_6+) » 1,000], with a typically light δ^{13}C-CH_4 (<−60‰ to −70‰) isotopic composition (45).

Analyses of the molecular and stable isotopic composition of hydrocarbon gases can often differentiate hydrocarbon gases of different thermal histories and genetic sources. Thermogenic hydrocarbon gases typically have higher concentrations of aliphatic hydrocarbons [e.g., ethane; (C_2H_6+/CH_4) > 1%, where C_2H_6+ denotes the contributions from ethane, propane, and higher order hydrocarbons] and heavier stable isotopic compositions than biogenic gas (CH_4 with a δ^{13}C-CH_4 > −55‰, typically −50‰ to −28‰) (45). However, the composition of thermogenic gases evolves as the organic source (i.e., kerogen or liquid hydrocarbons) degrades (45). As organic matter cracks to form oil and then hydrocarbon gas, the gases are initially enriched in higher aliphatic hydrocarbons [e.g., propane (C_3H_8) > ethane (C_2H_6) > methane (CH_4); termed wet gas] and ^{12}C (i.e., lighter δ^{13}C-CH_4). As thermal maturity increases, the heavier hydrocarbons are progressively broken down, increasing the CH_4/C_2H_6+ and δ^{13}C of various components (47). In most hydrocarbon gases, the isotopic composition (δ^{13}C-C_X) is δ^{13}C-C_3H_8 > δ^{13}C-C_2H_6 > δ^{13}C-CH_4 (47). However, in many thermally mature black shales, such as those observed in the MSA, this maturity trend reverses, creating diagnostic isotopic reversals in which the δ^{13}C-CH_4 becomes heavier than δ^{13}C-C_2H_6 [i.e., (δ^{13}C-CH_4 minus δ^{13}C-C_2H_6) = $\Delta C_{1\text{-}2}$ = >1) (3, 47). As a result, the analysis of compound specific isotopes can help to further constrain the potential sources of various thermally mature hydrocarbon gases (47–51).

Noble Gas Systematics. ***Background.*** Helium and the other noble gases are conservative tracers that are not altered by chemical or biological processes (e.g., bacterial reduction and oxidation). As a result, their original composition is preserved in shallow groundwaters independent of microbial activity or changes in oxygen fugacity. The well-characterized isotopic composition of major terrestrial reservoirs (i.e., mantle, crust, hydrosphere, and atmosphere) and coherent physico-chemical response to changing fluid conditions make noble gases uniquely valuable for constraining the source, mixing, mechanism of transport, and residence time of crustal fluids (52–56).

One of the unique advantages of applying noble gas geochemistry to groundwater studies is that the meteoric source for air-saturated water (ASW) is constant globally for both concentration and isotopic composition. As a result, the concentrations of ASW components in groundwater are a well-constrained function of temperature, salinity, and atmospheric pressure (elevation) (57, 58). Atmospheric noble gases (AIR) dissolve in groundwater when meteoric water equilibrates with the atmosphere before recharge into the subsurface. This equilibration follows Henry's law, with solubility increasing with higher atomic mass: He < Ne < Ar < Kr < Xe (57, 58).

Shallow groundwaters in unconfined aquifers typically have ASW noble gas composition characterized by near solubility levels of [^{4}He] (~40–45 × 10^{-6} cm^3 STP/L), [Ne] (175-220 × 10^{-6} cm^3 STP/L), and [Ar] (0.28–0.49 cm^3 STP/L) (57, 58). Isotopically, each gas component is similar to atmospheric compositions [i.e., helium: ^{3}He/^{4}He = 1.36×10^{-6} or ~0.985*Ra* (where *Ra* is the ratio of a sample relative to AIR = 1.39×10^{-6}); neon: ^{20}Ne/^{22}Ne (~9.8) and ^{21}Ne/^{22}Ne (~0.0289); and argon: ^{38}Ar/^{36}Ar (~0.188) and ^{40}Ar/^{36}Ar (~295.5)]. With the exception of helium (0.985*Ra*), the isotopic effect related to Henry's law solubility dissolution into meteoric water is less than the measurement error for Ne and Ar.

The second major source of noble gases in crustal fluids includes the isotopes produced in situ by radioactive decay. As hydrocarbon or meteoritic fluids interact with crustal fluids, the noble gas composition changes through the radiogenic nature and geologic history of the rocks through which fluids migrate within the Earth's crust (i.e., termed crustal gases) (37, 52, 53). Crustal gases are produced from the decay of $^{235;238}$U, ^{232}Th [^{4}He* (α-decay), and ^{21}Ne* (α-n reactions)], and K [^{40}Ar* (electron capture)] at known decay rates (59, 60). Marine sediments, such as black shales, are typically enriched in uranium content (specifically in comparison with thorium) as a result of uranium adsorption onto organic-rich particles during sediment deposition. In black shales, the typical range of concentrations are as follows: uranium (~1–30 ppm), thorium (~1–30 ppm), and ^{40}K (total K ~ 26,000 ppm, with a [^{40}K]/K ratio of 1.170×10^{-4} = ~3 ppm of ^{40}K of which 11% decays to ^{40}Ar*) (61). This radioactive decay leads to characteristic ratios of these radiogenic gases in crustal rocks such as thermally mature black shales (37). Typical isotopic ratios of crustal noble gases are ^{3}He/^{4}He = ~0.01*Ra*, ^{20}Ne/^{22}Ne (~9.7–10.0), ^{21}Ne/^{22}Ne (~0.029–0.060), and ^{40}Ar/^{36}Ar (~295.5–1,100), respectively (53).

Once radiogenic gases are formed in the crust, they are released from different lithologies at predictable and quantifiable rates as a function of formation temperature (i.e., release correlates to thermal maturity) (37, 62). Because of its small atomic radius, helium can diffuse through quartz on geologic time scales as short as decades, particularly at the elevated temperatures of hydrocarbon formations, and thus equilibrate with crustal fluids. Compared with heavier noble gases, helium is preferentially released from mineral grains in the crust. In general, helium (^{4}He*) content is higher in older formations and uranium-rich formations (e.g., black shales). Following catagenesis and metagenesis (conversion of organic kerogen to oil and then gas), helium is further enriched in hydrocarbon gases or other crustal fluids (water or oil) that experience significant migration (37, 54, 55, 63). The processes that enrich helium in migrating fluids result from the relatively lower solubility (higher partition coefficients) and high diffusivity of helium compared with methane or heavier noble gases in crustal fluids.

In comparison with ^{4}He, radiogenic ^{40}Ar (^{40}Ar*) is only released from crustal mineral grains into migrating fluids at higher temperatures (~220 °C) if K-rich feldspars present in crustal detritus break down or if K resides within exchangeable sites (i.e., clays) (37, 62). As a result, the relative ^{4}He/^{40}Ar* ratio is a sensitive marker for temperature-dependent release history of thermogenic hydrocarbon gas (37, 62).

Previous studies of the production and groundwater gas chemistry (in particular the helium and neon isotopic signatures) in the Appalachian Plateau and Fort Worth Basin have not revealed any detectable mantle contributions (37). As a result, the full suite of noble gas isotopic compositions in both basins (and

most groundwaters globally) reflects a well-constrained binary mixture of inert gases from two distinct sources: ASW and crustally produced isotopes. The resolution of these two components can be used to evaluate the different processes that control hydrocarbon gas and groundwater migration.

Groundwater–gas interactions. Groundwater transport plays a fundamental role in hydrocarbon gas migration [i.e., the methane saturation concentration or bubble point in fresh water at 10 °C is ~32–40 cm^3 STP/L at $p(CH_4)$ = 1 atm] and physically controls the migration of gases from and within hydrocarbon reservoirs (64–66). In fact, even if free gas-phase migration occurs, the methane will often redissolve back into crustal waters (e.g., formational brines or groundwater) when the free gas-phase enters groundwater that is undersaturated with respect to methane (55, 66).

The nucleation of a separate gas phase in groundwater occurs when the sum of the partial pressures of all dissolved gases (but generally dominated by a few major components such as CO_2 or CH_4) exceeds the hydrostatic pressure (the saturation point or sometimes called the bubble point). In cases where the partial pressure of dissolved methane is dominant, it controls the partitioning of trace gases (He, Ne, and Ar) because these trace components alone cannot attain (or sustain) sufficient partial pressures to nucleate or remain in the bubble phase even at the relatively low hydrostatic pressures present near the vadose zone. However, if any groundwater interacts with a free gas phase (e.g., CH_4), the trace gas components (e.g., ^4He, ^{20}Ne, ^{36}Ar, ^{40}Ar, and N_2) partition into the gas phase according to (*i*) their respective Bunsen solubility coefficients [β*x*, the ratio at equilibrium of the volume of dissolved gas *x* (at STP conditions) per unit volume of solution, when the partial pressure of *x* is 1 atmosphere] and (*ii*) the in situ volume ratio of gas to water (i.e., V_{gas}/V_{water}) (53, 67–69).

In low gas to water conditions (i.e., as V_{gas}/V_{water} approaches 0), trace gases with different solubilities will strongly fractionate as they partition from groundwater (dissolved) into the gas phase (54). In this scenario, the degree of molecular fractionation increases and can approach a maximum fractionation value of the ratio of their respective Bunsen coefficients (β_X/β_Y), termed α (assuming single stage fractionation; multistage fractionation can greatly exceed α). For example, the Bunsen coefficient ratio (α) for ^{20}Ne vs. ^{36}Ar (β_{Ne}/β_{Ar}) is ~3.7 at 10 °C, and for ^4He vs. CH_4 (β_{He}/β_{CH4}), it is ~4.7 at the same temperature. Conversely, for components with similar solubilities such as CH_4 vs. ^{36}Ar (β_{CH4}/β_{Ar}), α is about 1 at 10 °C (55, 66), and for ^4He vs. ^{20}Ne (β_{He}/β_{Ne}), α is about 1.2 at the same temperature (57, 58). These pairs of gases will partition into the gas phase according to V_{gas}/V_{water}, but will not experience significant molecular or isotopic fractionation relative to each other. As V_{gas}/V_{water} increases, the amount of dissolved gas that partitions into the gas phase will increase, whereas the degree of molecular (or isotopic) fractionation between gases with different solubilities decreases. Thus, in high V_{gas}/V_{water} conditions, nearly all of the trace gases will partition into the gas phase. In this case, even components with relatively large differences in solubility will not experience changes in molecular or isotopic ratios in either the gas or the residual water phases.

The saline spring at Salt Spring State Park, Montrose, PA, provides an appropriate analog for these processes. We sampled discharging water at this saline spring ~10 m below the water surface (within the steel pipe conduit in place since ~1900). The hydrocarbon gas, which is dominated by methane, remains dissolved in water as it is transported vertically to the surface. It is only when samples are collected at the surface that methane bubbles start to exsolve from the discharging brine.

A sample of the intact (undegassed) natural saline spring (collected ~10 m below water surface) has near saturation-level methane concentrations of 40.8 cm^3 STP/L and ASW solubility levels of $[^{20}Ne] = 312 \times 10^{-6}$ cm^3 STP/L and $[^{36}Ar] = 1{,}017 \times 10^{-6}$ cm^3 STP/L, with $[^4He] = 0.079$ cm^3 STP/L. The relevant gas ratios for the intact sample were $CH_4/^{36}Ar$ of $\sim 4.0 \times 10^4$ [or $p(CH_4)$ = ~1.1 atm], $^{20}Ne/^{36}Ar$ = 0.307, and $^4He/CH_4$ = 1,945 × 10^{-6}. For comparison, we collected the exsolved gas phase and residual water phase after gas exsolution at the surface. Both phases show a nearly identical $CH_4/^{36}Ar$ of $\sim 4.2 \times 10^4$. Although the $CH_4/^{36}Ar$ ratios in the two phases are the same, the CH_4 and ^{36}Ar concentrations in the residual liquid phase are only ~50% of the levels ($[CH_4]$ = 25.54 cm^3 STP/L and $[^{36}Ar] = 608 \times 10^{-6}$ cm^3 STP/L) measured in the intact sample. Similarly, the residual water phase had $[^4He]$ = 0.0045 cm^3 STP/L and $[^{20}Ne] = 79 \times 10^{-6}$ cm^3 STP/L, with $^{20}Ne/^{36}Ar$ of 0.13 and $^4He/CH_4 = 176 \times 10^{-6}$. These variations occur because CH_4 and some of the noble gases have been transferred from water-phase to gas-phase methane bubbles. The captured gas phase contained $[CH_4] = 0.682$ cm^3 STP/cm^3, $[^4He] = 0.00254$ cm^3 STP/cm^3, $[^{20}Ne] = 657 \times 10^{-6}$ cm^3 STP/cm^3, and $[^{36}Ar] = 1{,}926 \times 10^{-6}$ cm^3 STP/cm^3, with $^{20}Ne/^{36}Ar$ = 0.341 and $^4He/CH_4$ = 3,728 (×10^{-6}). The addition of 27 cm^3 STP of the exsolved gas to 1 L of the residual water predicts the concentrations observed in the single phase fluid to within 6%.

Numerical modeling. When combined, noble gases and the molecular and stable isotopic compositions of gas-phase hydrocarbons provide powerful tracers of crustal fluid processes (37, 54). Previous work demonstrates that solubility partitioning controls the postgenetic modification of natural CO_2 gas compositions in the crust (54, 63, 70). To evaluate the subsurface conditions present during isotopic and molecular fractionation of hydrocarbon gases, we adapt solubility fractionation models (54, 70, 71) for hydrocarbon gases.

We use numerical modeling to constrain the mechanisms and conditions under which hydrocarbon gas was transported to shallow aquifers (dashed lines in Fig. 4*A*). By applying solubility fractionation models to determine the subsurface conditions of the gas–water interactions, we are able to differentiate among the potential mechanisms of fugitive gas migration within aquifers overlying unconventional energy fields. In both the MSA and BSA, mantle contributions are minimal [i.e., crustal $^3He/^4He$ = 0.01–0.02R_A, where R_A is the helium isotope ratios of air and the neon isotopic signature is distinctly atmospheric ($^{20}Ne/^{22}Ne$ = 9.72–9.89 and $^{21}Ne/^{22}Ne$ = 0.028–0.030)]. Similarly, there is no evidence for oil-phase hydrocarbons within the localized geographic areas of either study area. As a result, solubility-controlled fractionation processes likely account for the ranges of $^4He/CH_4$ and $^{20}Ne/^{36}Ar$ data in both shale-gas fields.

The initial ASW is consistent with recently recharged meteoric water. Groundwater recharged under these conditions is assumed to have a salinity of zero and to have equilibrated at ~10 °C at an elevation of 600 m for Pennsylvania and at 20 °C with an elevation of 325 m for Texas (i.e., present day equilibration conditions for shallow groundwater in both locations). Under these conditions, the ^{20}Ne and ^{36}Ar in ASW are 171×10^{-6} cm^3 STP/L and $1{,}223 \times 10^{-6}$ cm^3 STP/L (PA) and 177×10^{-6} cm^3 STP/L and $1{,}267 \times 10^{-6}$ cm^3 STP/L (TX), respectively. Because all groundwater wells were sampled at depths <90 m, Bunsen solubility constants (β values: e.g., β_{Ne}/β_{Ar}) were not corrected for geothermal gradients. The Bunsen solubility constants for the noble gases are determined using refs. 57, 58, and 72, whereas the partition coefficients (α) are calculated following refs. 53 and 72.

The two-stage groundwater gas stripping and redissolution (GGS-R) model, as outlined in refs. 54, 70, and 71, postulates that trace gas components are extracted from the water phase in equilibrium with a gas phase through gas stripping. In our model, the gas stripping would occur by the continuous percolation of a methane gas phase. The gas phase would then contain crustal and ASW noble gases with the relative partitioning between the phases dependent on the relative β_X/β_Y and V_{gas}/V_{water} (53). As the gas migrates into groundwater containing gas levels below methane saturation, there is a partial redissolution of methane and the previously exsolved components back into groundwater (54, 71).

This latter transfer process is hypothesized for a subset of four impacted groundwater samples from Pennsylvania (Fig. 4*A*, *Upper Right*). The ASW noble gas composition of these samples plots as a mixture of stripped ASW water with ^{20}Ne and ^{36}Ar both equal to 0 (i.e., completely stripped) that mixes with small but variable amounts of a migrated gas phase with $^{20}Ne/^{36}Ar$ of ~1.5. The $CH_4/^{36}Ar$ ratio for these samples approaches Marcellus-produced gases. The added migrated ^{20}Ne and ^{36}Ar are likely incorporated as migrated hydrocarbon gas dissolves into the groundwater until reaching methane saturation.

1. Engelder T, Lash GG, Uzcategui RS (2009) Joint sets that enhance production from Middle and Upper Devonian gas shales of the Appalachian Basin. *AAPG Bull* 93(7): 857–889.
2. Rast N, ed (1989) *The Evolution of the Appalachian Chain* (Geological Society of America, Denver), Vol A, pp 347–358.
3. Burruss RC, Laughrey CD (2010) Carbon and hydrogen isotopic reversals in deep basin gas: Evidence for limits to the stability of hydrocarbons. *Org Geochem* 41(12):1285–1296.
4. Lash GG, Engelder T (2009) Tracking the burial and tectonic history of Devonian shale of the Appalachian Basin by analysis of joint intersection style. *Geol Soc Am Bull* 121(1-2):265–277.
5. Faill RT (1997) A geologic history of the north-central Appalachians. 1. Orogenesis from the mesoproterozoic through the taconic orogeny. *Am J Sci* 297(6):551–619.
6. Faill RT (1997) A geologic history of the north-central Appalachians. 2. The Appalachian basin from the Silurian through the Carboniferous. *Am J Sci* 297(7):729–761.
7. Sak PB, McQuarrie N, Oliver BP, Lavdovsky N, Jackson MS (2012) Unraveling the central Appalachian fold-thrust belt, Pennsylvania: The power of sequentially restored balanced cross sections for a blind fold-thrust belt. *Geosphere* 8(3):685–702.
8. Scanlin MA, Engelder T (2003) The basement versus the no-basement hypotheses for folding within the Appalachian plateau detachment sheet. *Am J Sci* 303(6):519–563.
9. Davis DM, Engelder T (1985) The role of salt in fold-and-thrust belts. *Tectonophysics* 119(1-4):67–88.
10. Milici RC, Witt WD (1988) The Appalachian Basin. *The Geology of North America* (Geological Society of America, Denver), pp 427–469.
11. Frey MG (1973) Influence of Salina salt on structure in New York-Pennsylvania part of the Appalachian Plateau. *Am Assoc Pet Geol Bull* 57(6):1027–1037.
12. Ryder RT, et al. (1996) Possible continuous-type (unconventional) gas accumulation in the Lower Silurian "Clinton" sands, Medina Group, and Tuscarora Sandstone in the Appalachian basin: A progress report of 1995 activities. *USGS Open-File Report 96-42* (United States Geological Survey, Washington, DC).
13. Straeten CAV, Brett CE, Sageman BB (2011) Mudrock sequence stratigraphy: A multiproxy (sedimentological, paleobiological and geochemical) approach, Devonian Appalachian Basin. *Palaeogeogr Palaeoclimatol Palaeoecol* 304(1-2):54–73.
14. Engelder T, Whitaker A (2006) Early jointing in coal and black shale: Evidence for an Appalachian-wide stress field as a prelude to the Alleghanian orogeny. *Geology* 34(7): 581–584.
15. Bofinger VM, Compston W (1967) A reassessment of age of Hamilton Group in New York and Pennsylvania and role of inherited radiogenic Sr-87. *Geochim Cosmochim Acta* 31(12):2353–2357.
16. Taylor L (1984) *Groundwater Resources of the Upper Susquehanna River Basin, Pennsylvania: Water Resources Report 58* (Pennsylvania Department of Environmental Resources, Office of Parks and Forestry, Bureau of Topographic and Geologic Survey, Harrisburg, PA), p 136.
17. Evans MA (1995) Fluid inclusions in veins from the Middle Devonian shales- A record of deformation conditions and fluid evolution in the Appalachian Plateau. *Geol Soc Am Bull* 107(3):327–339.
18. Bethke CM, Marshak S (1990) Brine migrations across North America: The plate-tectonics of groundwater. *Annu Rev Earth Planet Sci* 18:287–315.
19. Oliver J (1986) Fluids expelled tectonically from orogenic belts- Their role in hydrocarbon migration and other geologic phenomena. *Geology* 14(2):99–102.
20. Engelder T (2008) Structural geology of the Marcellus and other Devonian gas shales: Geological conundrums involving joints, layer-parallel shortening strain, and the contemporary tectonic stress field. *AAPG-SEG Eastern Section Meeting Field Trip Guide* (American Association of Petroleum Geology, Tulsa, OK).
21. Pollastro RM, Jarvie DM, Hill RJ, Adams CW (2007) Geologic framework of the Mississippian Barnett Shale, Barnett-Paleozoic total petroleum system, bend arch-Fort Worth Basin, Texas. *AAPG Bull* 91(4):405–436.
22. Walper JL (1982) Plate tectonic evolution of the Fort Worth Basin. *Petroleum geology of the Fort Worth Basin and Bend Arch Area*, ed Martin CA (Dallas Geological Society, Dallas), pp 237–251.
23. Flippin JW (1982) The stratigraphy, structure, and economic aspects of the Paleozoic strata in Erath county, north central Texas. *Petroleum Geology of the Fort Worth Basin and Bend Arch Area*, ed Martin CA (Dallas Geological Society, Dallas), pp 129–155.
24. Hill RJ, Jarvie DM, Zumberge J, Henry M, Pollastro RM (2007) Oil and gas geochemistry and petroleum systems of the Fort Worth Basin. *AAPG Bull* 91(4):445–473.
25. Henry JD (1982) Stratigraphy of the Barnett shale (Mississippian) and associated reefs in the northern Fort Worth Basin. *Petroleum Geology of the Fort Worth Basin and Bend Arch Area*, ed Martin CA (Dallas Geological Society, Dallas), pp 157–178.
26. Hill RJ, Jarvie DM, Pollastro RM, Bowker KA, Claxton BL (2004) Geochemistry of an unconventional gas prospect: The Barnett Shale gas model. *Geochim Cosmochim Acta* 68(11):A231–A231.
27. Montgomery SL, Jarvie DM, Bowker KA, Pollastro RM (2005) Mississippian Barnett Shale, Fort Worth basin, north-central texas: Gas-shale play with multi-trillion cubic foot potential. *AAPG Bull* 89(2):155–175.
28. Bowker KA (2007) Barnett Shale gas production, Fort Worth Basin: Issues and discussion. *AAPG Bull* 91(4):523–533.
29. Jarvie DM, Hill RJ, Ruble TE, Pollastro RM (2007) Unconventional shale-gas systems: The Mississippian Barnett Shale of north-central Texas as one model for thermogenic shale-gas assessment. *AAPG Bull* 91(4):475–499.
30. Rodriguez ND, Philp RP (2010) Geochemical characterization of gases from the Mississippian Barnett Shale, Fort Worth Basin, Texas. *AAPG Bull* 94(11):1641–1656.
31. Kornacki AS, McCaffrey MA (2011) *Applying Geochemical Fingerprinting Technology to Determine the Source of Natural Gas Samples Obtained from Water Wells in Parker County and Hood County* (Weatherford Laboratories, Houston).
32. Barker RA, Ardis AF (1992) Configuration of the base of the Edwards-Trinity aquifer system and hydrogeology of the underlying pre-Cretaceous rocks, West-Central Texas. *Water Resources Investigations Report* (US Geological Survey, Austin, TX).
33. Warner NR, et al. (2012) Geochemical evidence for possible natural migration of Marcellus Formation brine to shallow aquifers in Pennsylvania. *Proc Natl Acad Sci USA* 109(30):11961–11966.
34. Osborn SG, Vengosh A, Warner NR, Jackson RB (2011) Methane contamination of drinking water accompanying gas-well drilling and hydraulic fracturing. *Proc Natl Acad Sci USA* 108(20):8172–8176.
35. Jenden PD, Drazan DJ, Kaplan IR (1993) Mixing of thermogenic natural gases in the Northern Applachian Basin *AAPG Bull* 77(6):980–998.
36. Laughrey CD, Baldassare FJ (1998) Geochemistry and origin of some natural gases in the Plateau province, central Appalachian basin, Pennsylvania and Ohio. *Aapg Bulletin-American Association of Petroleum Geologists* 82(2):317–335.
37. Hunt AG, Darrah TH, Poreda RJ (2012) Determining the source and genetic fingerprint of natural gases using noble gas geochemistry: A northern Appalachian Basin case study. *AAPG Bull* 96(10):1785–1811.
38. Molofsky LJ, Connor JA, Wylie AS, Wagner T, Farhat SK (2013) Evaluation of methane sources in groundwater in northeastern Pennsyvlania. *Ground Water* 51(3):333–349.
39. Jackson RB, et al. (2013) Increased stray gas abundance in a subset of drinking water wells near Marcellus shale gas extraction. *Proc Natl Acad Sci USA* 110(28): 11250–11255.
40. Darrah TH, et al. (2013) Gas chemistry of the Dallol region of the Danakil Depression in the Afar region of the northern-most East African Rfit. *Chem Geol* 339(Frontiers in Gas Geochemistry):16–29.
41. USGS (2011) *National Field Manual for the Collection of Water-Quality Data* (US Geological Survey, Washington, DC).
42. Isotech (2011) *Collection of Groundwater Samples from Domestic and Municipal Water Wells for Dissolved Gas Analysis* (Isotech Laboratories, Champaign, IL).
43. Dowling CB, Poreda RJ, Hunt AG, Carey AE (2004) Ground water discharge and nitrate flux to the Gulf of Mexico. *Ground Water* 42(3):401–417.
44. Solomon DK, Poreda RJ, Cook PG, Hunt A (1995) Site characterization using H-3/He-3 groundwater ages, Cape Cod, MA. *Ground Water* 33(6):988–996.
45. Schoell M (1983) Genetic characterization of natural gases. *AAPG Bull* 67(12): 2225–2238.
46. Whiticar MJ, Faber E, Schoell M (1986) Biogenic methane formation in marine and fresh-water environments- CO2 reduction vs acetate fermentation isotope evidence. *Geochim Cosmochim Acta* 50(5):693–709.
47. Tilley B, et al. (2011) Gas isotope reversals in fractured gas reservoirs of the western Canadian Foothills: Mature shale gases in disguise. *AAPG Bull* 95(8):1399–1422.
48. Tilley B, Muehlenbachs K (2013) Isotope reversals and universal stages and trends of gas maturation in sealed, self-contained petroleum systems. *Chem Geol* 339:194–204.
49. Tilley B, Muehlenbachs K (2006) Gas maturity and alteration systematics across the Western Canada Sedimentary Basin from four mud gas isotope depth profiles. *Org Geochem* 37(12):1857–1868.
50. Tilley B, Muehlenbachs K (2012) Fingerprinting of gas contaminating groundwater and soil in a petroliferous region, Alberta, Canada. *Environmental Forsenics, Proceedings of the 2011 INEFF Conference* (Royal Society of Chemistry, London), pp 115–125.
51. Rowe D, Muehlenbachs K (1999) Isotopic fingerprints of shallow gases in teh Western Canadian Sedimentary Basin: Tools for remediation of leaking heavy oil wells. *Org Geochem* 30(8):861–871.
52. Solomon DK, Hunt A, Poreda RJ (1996) Source of radiogenic helium 4 in shallow aquifers: Implications for dating young groundwater. *Water Resour Res* 32(6): 1805–1813.
53. Ballentine CJ, Burgess R, Marty B (2002) Tracing fluid origin, transport and interaction in the crust. *Noble Gases in Geochemistry and Cosmochemistry*, eds Porcelli D, Ballentine CJ, Wieler R (Mineralogical Society of America, Washington, DC), Vol 47, pp 539–614.
54. Gilfillan SMV, et al. (2009) Solubility trapping in formation water as dominant CO2 sink in natural gas fields. *Nature* 458(7238):614–618.
55. Lollar BS, Ballentine CJ (2009) Insights into deep carbon derived from noble gases. *Nat Geosci* 2(8):543–547.
56. Solomon DK, Poreda RJ, Schiff SL, Cherry JA (1992) Tritium and He-3 as groundwater age tracers in the Borden Aquifer. *Water Resour Res* 28(3):741–755.
57. Weiss R (1971) Effect of salinity on the solubility of argon in water and seawater. *Deep-Sea Res* 18(2):225–230.
58. Weiss R (1971) Solubility of helium and neon in water and seawater. *J Chem Eng Data* 16(2):235–241.

59. Wetherill GW (1954) Variations in the isotopic abundances of neon and argon extracted from radioactive materials. *Phys Rev* 96(11):679–683.
60. Wetherill GW, Wasserburg GJ, Aldrich LT, Tilton GR, Hayden RJ (1956) Decay Constants of K-40 as determined by the radiogenic argon content of potassium minerals. *Phys Rev* 103(4):987–989.
61. Taylor SR, McLennan SM (1995) The geochemical evolution of the continental crust. *Rev Geophys* 33:241–265.
62. Ballentine CJ, Mazurek M, Gautschi A (1994) Thermal constraints on crustal rare-gas release and migration-Evidence from Alpine fluid inclusions. *Geochim Cosmochim Acta* 58(20):4333–4348.
63. Dubacq B, et al. (2012) Noble gas and carbon isotopic evidence for CO2-driven silicate dissolution in a recent natural CO2 field. *Earth Planet Sci Lett* 341:10–19.
64. Ballentine CJ, O'Nions RK (1994) The use of He, Ne, and Ar isotopes to study hydrocarbon related fluid provenance, migration, mass balance in sedimentary basins. *Geofluids: Origin, Migration, and Mass Balance in Sedimentary Basins*, ed Parnell J (Geological Society of London, London), pp 347–361.
65. Cathles LM (1990) Scales and effects of fluid-flow in the upper crust. *Science* 248(4953):323–329.
66. Ballentine CJ, et al. (1991) Rare-gas constraints on hydrocarbon accumulation, crustal degassing and groundwater-flow in the Pannonian Basin. *Earth Planet Sci Lett* 105(1-3):229–246.
67. Aeschbach-Hertig W, El-Gamal H, Wieser M, Palcsu L (2008) Modeling excess air and degassing in groundwater by equilibrium partioning with a gas phase. *Water Resour Res* 44(8):W08449.
68. Holocher J, Peeters F, Aeschbach-Hertig W, Kinzelbach W, Kipfer R (2003) Kinetic model of gas bubble dissolution in groundwater and its implications for the dissolved gas composition. *Environ Sci Technol* 37(7):1337–1343.
69. Aeschbach-Heritg W, Peeters F, Beyerle U, Kipfer R (1999) Interpretation of dissolved atmospheric noble gase in natural waters. *Water Resour Res* 35(9):2779–2792.
70. Zhou Z, Ballentine CJ, Schoell M, Stevens SH (2012) Identifying and quantifying natural CO2 sequestration processes over geological timescales: The Jackson Dome CO2 Deposit, USA. *Geochim Cosmochim Acta* 86:257–275.
71. Gilfillan SM, et al. (2008) The noble gas geochemistry of natural CO2 gas reservoirs from the Colorado Plateau and Rocky Mountain provinces, USA. *Geochim Cosmochim Acta* 72(4):1174–1198.
72. Smith SP, Kennedy BM (1982) The solubility of noble gases in water and in NaCl brine. *Geochim Cosmochim Acta* 47(3):503–515.

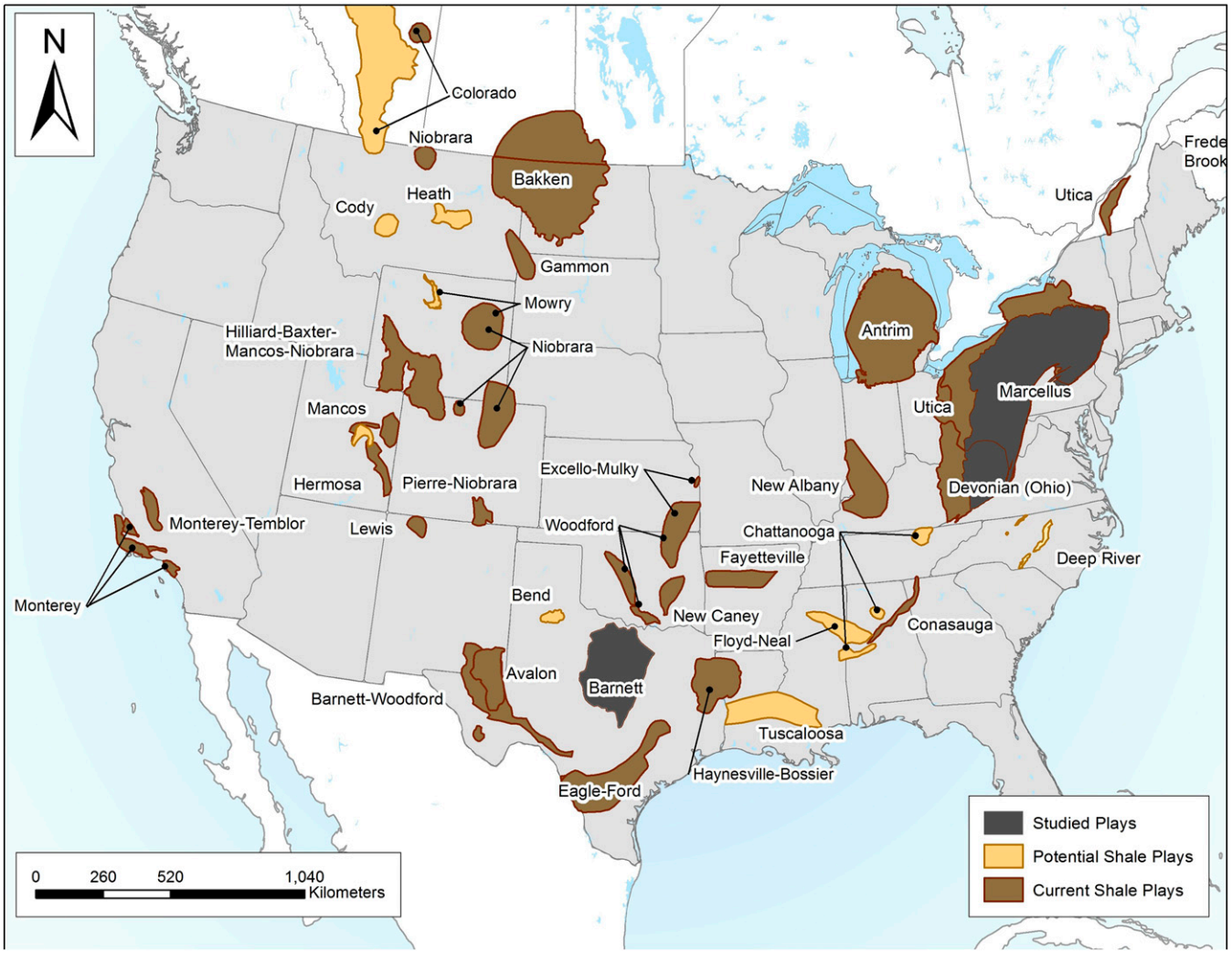

Fig. S1. A geographic map of current (brown) and potential (orange) shale gas plays across the lower 48 United States. Groundwater samples overlying the Barnett and Marcellus study areas are included in this study (black) (1).

1. US Energy Information Administration (2013) *Annual Energy Outlook 2014* (USEIA, Washington, DC).

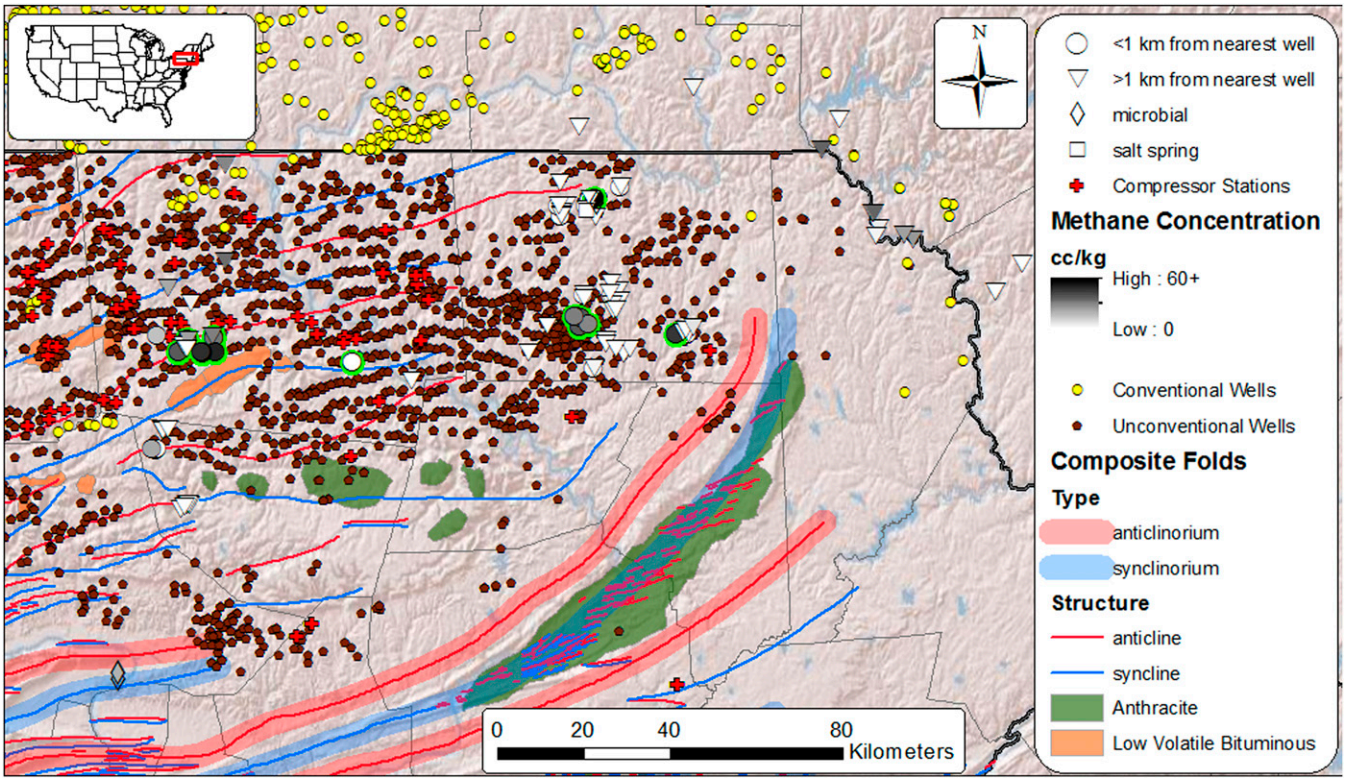

Fig. S2. Sampling locations within the MSA are collected from northeastern Pennsylvania and southern New York. The background topographic map and geological features were downloaded from http://www.pasda.psu.edu/, the Carnegie Museum of Natural History, and refs. 1 and 2. The locations of conventional and unconventional wells were sourced from the Pennsylvania Department of Environmental Protection's Oil and Gas reporting website (www.paoilandgasreporting.state.pa.us) and the Division of Mineral Resources of New York State's Department of Environmental Conservation (www.dec.ny.gov/cfmx/extapps/GasOil/).

1. Faill RT (2011) *Folds of Pennsylvania: GIS Data and Map* (Survey PG).
2. East JA (2013) *Coal Fields of the Conterminous United States: National Coal Resource Assessment* (US Geological Survey, Reston, VA).

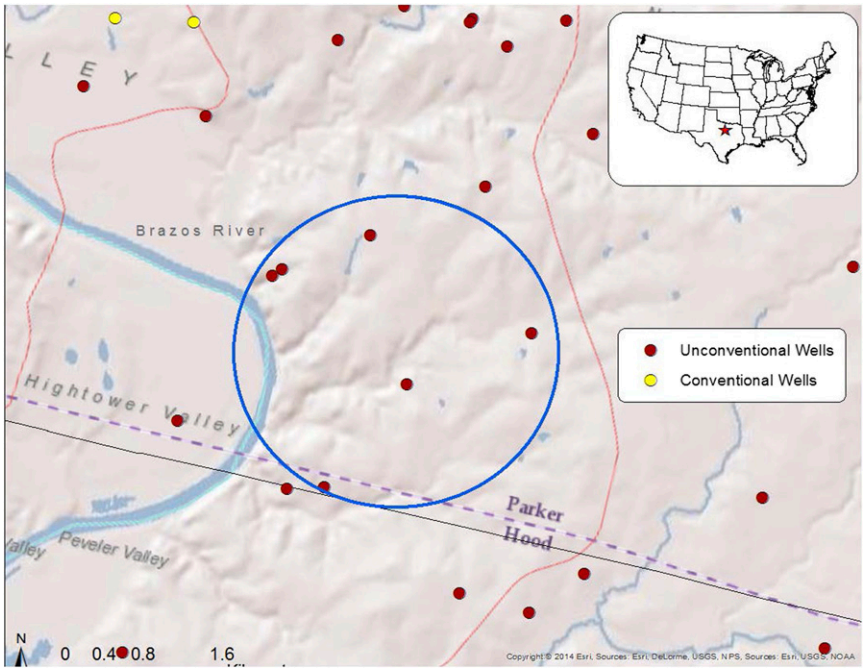

Fig. S3. Groundwater sampling locations from Upper Trinity aquifer within the Barnett Study area of east-central Texas. The background topographic map, geological features, and the locations of conventional and unconventional wells were sourced from the Texas Railroad Commission (wwwgisp.rrc.state.tx.us/GISViewer2/ and www.rrc.state.tx.us/about-us/resource-center/research/data-sets-available-for-purchase/digital-map-data/).

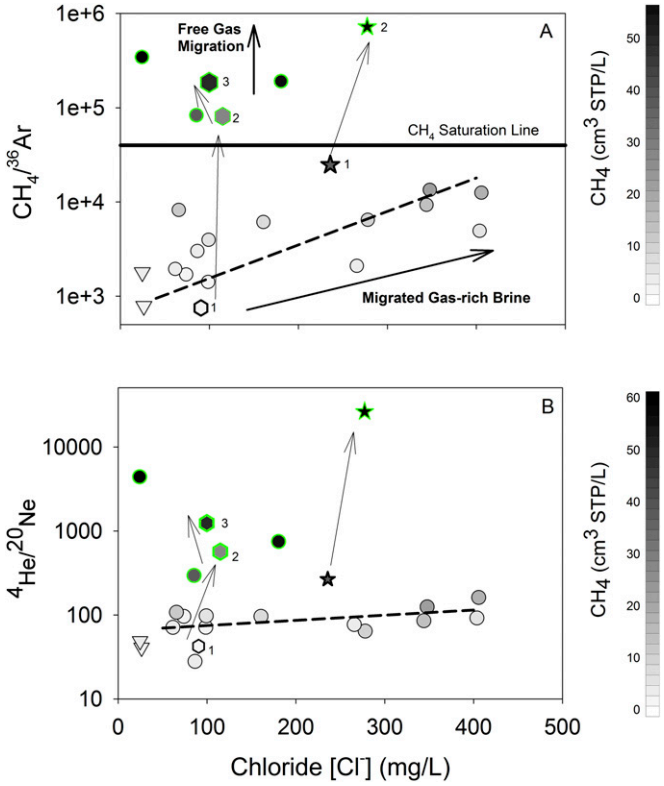

Fig. S4. The $CH_4/^{36}Ar$ (*Upper*) and $^4He/^{20}Ne$ (*Lower*) ratios vs. chloride (Cl^-) of domestic drinking-water wells overlying BSA at distances >1 km (triangles) and <1 km (circles) from unconventional shale-gas wells (Table S2). [CH_4] is shown using grayscale intensity [0–60^+ cm^3 ([CH_4]) STP/L] as scaled on white-black color bars. Fifteen samples from the BSA had [CH_4] at or below saturation and significant correlations between $CH_4/^{36}Ar$ ($r^2 = 0.59$; $P < 0.01$) and $^4He/^{20}Ne$ ($r^2 = 0.48$; $P < 0.01$) with Cl^- (Fig. 2 *C* and *D*). Five samples, including two samples [BSA-5 (tracked as squares) and BSA-8 (tracked as diamonds)] displayed pronounced changes between the first and second two sampling events and have substantially higher $CH_4/^{36}Ar$ and $^4He/^{20}Ne$ independent of [Cl^-] (green-rimmed circles). The subset of samples from both locations that have elevated CH_4 and do not fall along the normal trend regression lines are consistent with a flux of gas-phase thermogenic hydrocarbon gas into shallow aquifers. The changes between the initial and subsequent collection periods for samples BSA-5 (hexagon) and BSA-8 (diamond) are tracked by following the arrows. Notice in both cases how the ratio of thermogenic to ASW gases increased following the initial sampling periods.

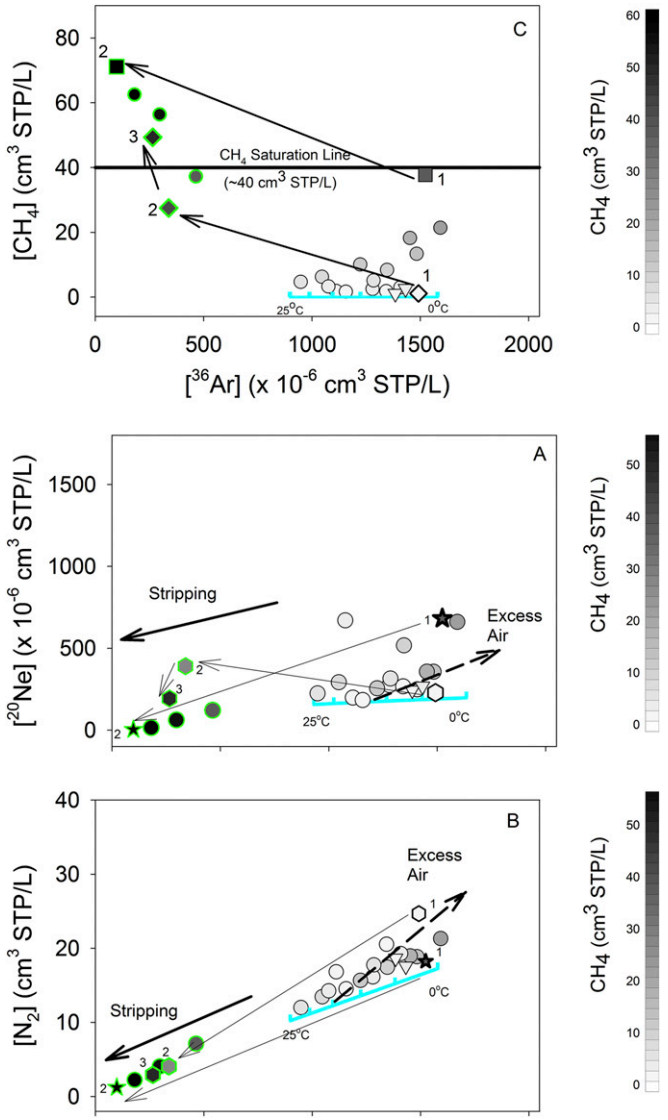

Fig. S5. ^{20}Ne (*Top*), N_2 (*Middle*), and CH_4 (*Bottom*) vs. ^{36}Ar in the BSA at distances >1 km (triangles) and <1 km (circles) from drill sites. In natural groundwaters, the concentration of ASW gases (e.g., ^{20}Ne, ^{36}Ar, and N_2) is determined by their solubility during groundwater recharge (1, 2) with minor additions of excess air (with atmospheric composition) that is trapped during the recharge process (3). Most samples (15 of 20) in the BSA have normal ASW composition (Fig. 3 *D–F*), but 5 anomalous samples, including 2 samples [BSA-5 (tracked as squares) and BSA-8 (tracked as diamonds)] that displayed pronounced changes between the initial and later sampling events, have significantly stripped ASW gas composition (green-rimmed circles). The changes between the initial and subsequent collection periods for samples BSA-5 (hexagon) and BSA-8 (diamond) are tracked by following the arrows. In both cases, notice how the samples progressed from normal to stripped ASW composition with increasing $[CH_4]$.

1. Weiss R (1971) Effect of salinity on the solubility of argon in water and seawater. *Deep-Sea Res* 18(2):225–230.
2. Weiss R (1971) Solubility of helium and neon in water and seawater. *J Chem Eng Data* 16(2):235–241.
3. Heaton THE, Vogel JC (1981) Excess air in groundwater. *J Hydrol (Amst)* 50(1-3):201–216.

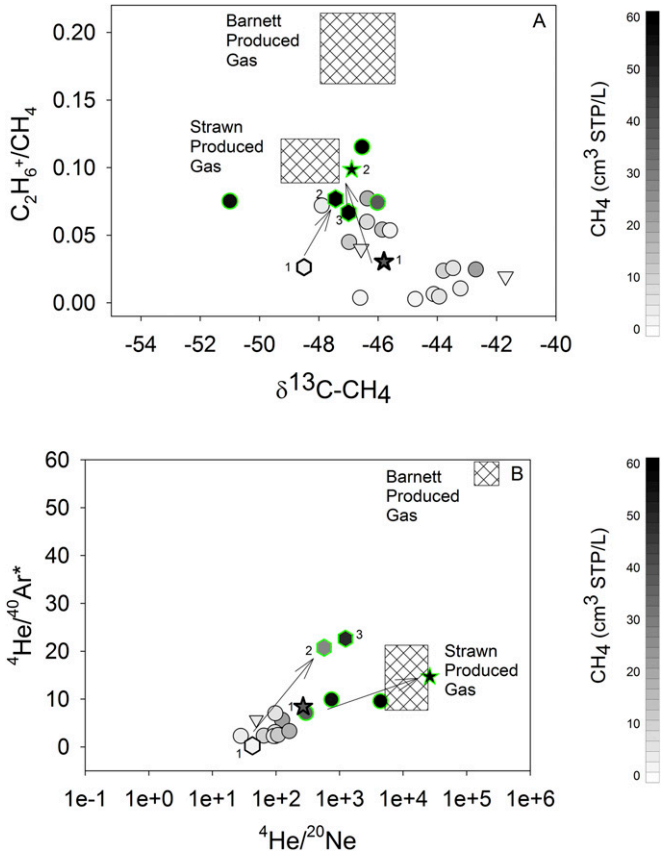

Fig. S6. C_2H_6+/CH_4 vs. $\delta^{13}C\text{-}CH_4$ (*Upper*) and $^4He/^{40}Ar^*$ vs. $^4He/^{20}Ne$ (*Lower*) in groundwater and produced gases from the BSA. Samples collected >1 and <1 km from drill sites are shown as triangles and circles, respectively. The Strawn and Barnett ranges include data reported in ref. 1 or collected as part of the present study (Table S3). Although the $\delta^{13}C\text{-}CH_4$ does not unambiguously distinguish the source of hydrocarbons in this setting, the molecular ratio of aliphatic hydrocarbons (C_2H_6+/CH_4) is consistent with local Strawn production gases, specifically in the most gas-rich groundwaters with evidence of gas-phase migration and stripping. Similarly, this subset of groundwaters has elevated $^4He/^{40}Ar^*$ and $^4He/^{20}Ne$ significantly above the natural groundwaters in the area. The similarity between these proxies for the five impacted wells, including the two that displayed pronounced changes between the first and second two samplings, suggests an intermediate depth Strawn gas (scenario 4: annulus leakage) as the most likely cause for the fugitive gas contamination observed in Texas. The changes between the initial and subsequent collection periods for samples BSA-5 (hexagon) and BSA-8 (diamond) are tracked by following the arrows. In both cases, notice how the data progress toward Strawn produced gases.

1. Kornacki AS, McCaffrey MA (2011) *Applying Geochemical Fingerprinting Technology to Determine the Source of Natural Gas Samples Obtained from Water Wells in Parker County and Hood County* (Weatherford Laboratories, Houston).

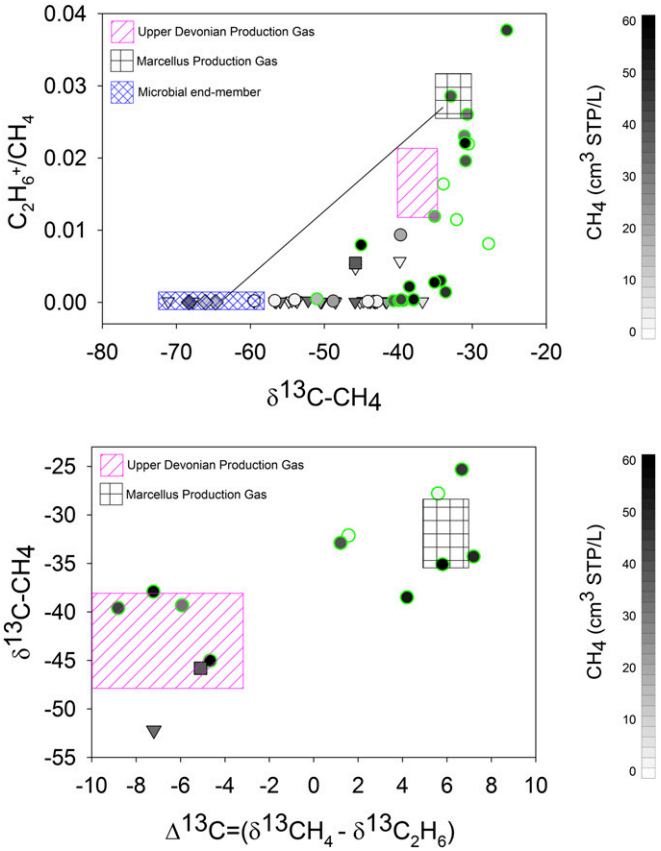

Fig. S7. The ratio of ethane plus higher order hydrocarbons to methane (C_2H_6+/CH_4) plotted against $\delta^{13}C\text{-}CH_4$ (*Upper*) and isotope signatures of methane ($\delta^{13}C\text{-}CH_4$) vs. [methane ($\delta^{13}C\text{-}CH_4$) minus ethane ($\delta^{13}C\text{-}C_2H_6$) ($\Delta^{13}C = \delta^{13}C\text{-}CH_4\text{-}\delta^{13}C\text{-}C_2H_6$)] (*Lower*) in drinking-water wells from MSA collected at distances >1 km (triangles) and <1 km (circles) from drill sites. The natural Salt Spring, Montrose, PA, is shown as a square and samples targeted for microbial-sourced gases are distinguished by diamonds. Notice that in the MSA, the samples with elevated [CH_4] and stripped ASW composition (green-rimmed circles) tend to have elevated C_2H_6+/CH_4 and "heavier" $\delta^{13}C\text{-}CH_4$ compared with the majority of samples >1 km from drilling. Once a fugitive gas is identified, a comparison of fingerprints such as C_2H_6+/CH_4 vs. $\delta^{13}C\text{-}CH_4$ can differentiate the source of leakage. For example, Marcellus-produced gases have higher C_2H_6+/CH_4 (typically >0.015) and heavier $\delta^{13}C\text{-}CH_4$ (−29‰ to −35‰) (black box) than UD production gases [i.e., lower C_2H_6+/CH_4 (typically C_2H_6+/CH_4 <0.015) and lighter $\delta^{13}C\text{-}CH_4$ (<∼−38‰)] (pink box) (1–3). Compound specific isotopes such as $\delta^{13}C\text{-}CH_4$ vs. $\Delta^{13}C$ can also help to differentiate the source of leakage. Four of the 12 drinking-water samples analyzed for compound specific isotopic analysis are consistent with Marcellus production gases [$\delta^{13}C\text{-}CH_4 > \sim-35‰$ (−29‰ to −35‰) and $\Delta^{13}C > 0$] (2). Conversely, 5 of 12 and the saline spring at Salt Spring State Park had $\delta^{13}C\text{-}CH_4$ consistent with Upper Devonian production gases [$\delta^{13}C\text{-}CH_4 < \sim-38‰$ (∼38‰ to −44‰) and $\Delta^{13}C < 0$], whereas 73 samples exhibited intermediate composition that includes a partial isotopic reversal (2).

1. Molofsky LJ, Connor JA, Wylie AS, Wagner T, Farhat SK (2013) Evaluation of methane sources in groundwater in northeastern Pennsyvlania. *Ground Water* 51(3):333–349.
2. Jackson RB, et al. (2013) Increased stray gas abundance in a subset of drinking water wells near Marcellus shale gas extraction. *Proc Natl Acad Sci USA* 110(28):11250–11255.
3. Baldassare FJ, McCaffrey MA, Harper JA (2014) A geochemical context for stray gas investigations in the northern Appalachian Basin: Implications of analyses of natural gases from Neogene-through Devonian-age strata. *AAPG Bull* 98(2):341–372.

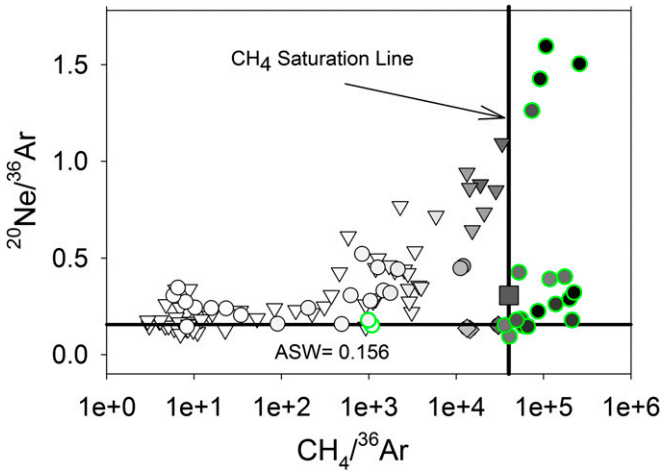

Fig. S8. A comparison of the $^{20}Ne/^{36}Ar$ and $CH_4/^{36}Ar$ ratios in the MSA at distances >1 km (triangles) and <1 km (circles) from drill sites. The natural Salt Spring, Montrose, PA, is shown as a square and samples targeted for microbial-sourced gases are distinguished by diamonds. Note that in the cohort of natural samples (<1 km from drill sites), the $^{20}Ne/^{36}Ar$ and total [^{20}Ne] (Table S1) increase with increasing [CH_4]. The simultaneous increase in $^{20}Ne/^{36}Ar$ and total [^{20}Ne] reflects the increasing contributions of additional exogenous ^{20}Ne with increasing quantities of migrated thermogenic hydrocarbon gas in the MSA.

Other Supporting Information Files

Table S1 (DOCX)
Table S2 (DOCX)
Table S3 (DOCX)